

OcclusionFormer: Arranging Z-Order for Layout-Grounded Image Generation

Ziye Li¹ Henghui Ding¹✉

Project Page: <https://henghuiding.com/OcclusionFormer/>

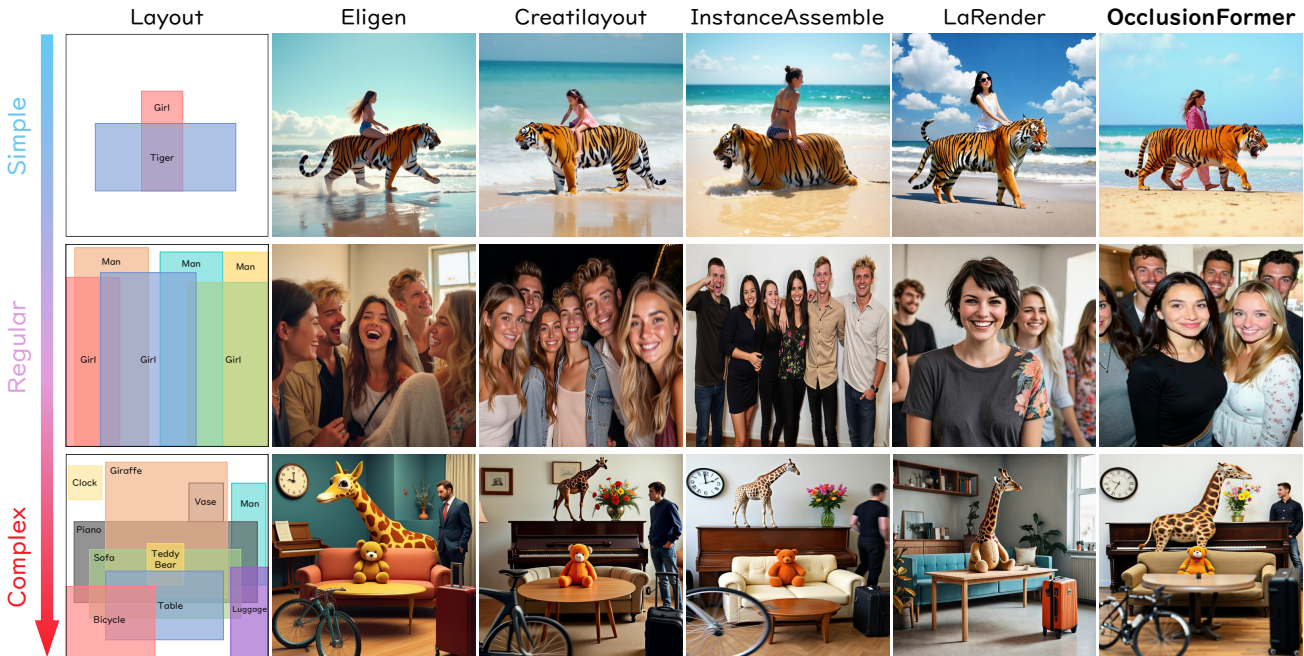


Figure 1. Comparison with state-of-art methods. The first column illustrates the layout condition with multiple bounding boxes and occlusion ordering (Z-order), where foreground boxes partially occlude background ones. The results demonstrate that the proposed OcclusionFormer consistently outperforms prior methods under both simple and complex overlap patterns.

Abstract

Recent layout-to-image models have achieved remarkable progress in spatial controllability. However, they still struggle with inter-object occlusion. When bounding boxes overlap, most existing methods lack explicit occlusion information, which makes the generation in intersection regions inherently ambiguous and hinders the determination of complex occlusion relationships. As a result, they often produce entangled textures or physically inconsistent layering in the overlapped areas. To address this issue, we first construct **SA-Z**, a large-scale dataset enriched with explicit

occlusion ordering and pixel-level annotations. Building upon our proposed dataset, we introduce **OcclusionFormer**, a novel occlusion-aware Diffusion Transformer framework that explicitly models Z-order priority by decoupling instances and compositing them via volume rendering. Furthermore, to ensure fine-grained spatial precision, we introduce a queried alignment loss that explicitly supervises individual instances and enhances semantic consistency. The proposed method effectively reduces ambiguity in overlapping regions, enforces correct occlusion dependencies, and preserves structural integrity, leading to substantial accuracy gains across diverse scenes.

¹Institute of Big Data, College of Computer Science and Artificial Intelligence, Fudan University, China. Correspondence to: Henghui Ding <henghui.ding@gmail.com>.

1. Introduction

Layout-to-image generation (Li et al., 2023) extends text-conditioned image generation by introducing explicit layout constraints, enabling finer-grained spatial controllability. By leveraging 2D/3D bounding boxes (Zhang et al., 2023; Li

et al., 2023; Zhou et al., 2024; Wang et al., 2024; Cheng et al., 2024; Zhang et al., 2025a;b; Xiang et al., 2025; Qin et al., 2025; He et al., 2025) or image signals (Lv et al., 2024; Li et al., 2025c;d; Sun et al., 2024; Chen et al., 2024; Lin et al., 2024; Mo et al., 2024) as spatial guidance, these methods allow users to specify object locations and scales with high precision. Such capability is important for applications requiring strong structural fidelity, such as complex scene composition and visual storytelling, where the intended spatial arrangement must be faithfully preserved.

However, most existing methods largely overlook the challenge of inter-object occlusion. Unlike computer graphics pipelines that use a Z-buffer to resolve occlusion, they lack an explicit *Z-order* that specifies the depth priority determining occlusion. While effective for isolated instances, these methods struggle with overlaps where intersecting boxes create ambiguity. Rather than resolving occlusion, they typically treat overlaps as feature mixtures, without explicitly distinguishing spatially overlapped instances. This can lead to entangled textures and physically inconsistent layering in the intersecting areas, ultimately harming visual realism.

This limitation also conflicts with the intuitive user workflow. As shown in Figure 1, users naturally provide amodal bounding boxes that specify the full object extent regardless of occlusion, rather than delineating only visible fragments. They then expect the model to follow their intended Z-order to resolve inter-object interactions. However, without explicit Z-order modeling, existing methods often misinterpret overlaps as conflicting spatial conditions and force objects to shrink into the visible area or merge unnaturally. These artifacts ultimately violate the user’s compositional intent.

A notable attempt to address this issue is LaRender (Zhan & Liu, 2025), which simulates occlusion via training-free volumetric rendering (Mildenhall et al., 2020). However, it repurposes the cross-attention space in the diffusion model for occlusion control, which prevents the use of global prompts. Furthermore, its heuristic latent manipulation is sensitive to hyperparameter choices, compromising spatial precision. As shown in Figure 1, LaRender may deviate from the specified layout under heavy overlaps, and its performance can drop in complex scenes where unsupervised guidance struggles to resolve complex occlusion dependencies.

To bridge this gap, we contend that data-driven explicit supervision is essential. We first construct *SA-Z*, a large-scale dataset enriched with detailed pixel-level captions and explicit Z-order annotations. Additionally, we leverage SAM-3D (Chen et al., 2025) to reconstruct 3D geometry and derive amodal annotations for occluded instances. Building on this foundation, we propose *OcclusionFormer*, a novel framework that learns to explicitly model Z-axis priority. By integrating volumetric rendering with instance decoupling, our approach resolves depth dependencies via transmittance

calculation, ensuring correct occlusion. Unlike previous heuristics, our approach maintains high fidelity even in challenging scenarios. Finally, while OverLayBench (Li et al., 2025b) serves as a valuable benchmark centered on occlusion, it relies on synthetic images. To address this domain gap, we curate a challenging real-world benchmark from our SA-Z to serve as a rigorous testbed for complex occlusion. Our main contributions are summarized as follows:

- We introduce *SA-Z*, a large-scale dataset enriched with detailed pixel-level instance captions and explicit Z-order annotations, and we further employ SAM-3D to derive amodal annotations via 3D reconstruction.
- We propose *OcclusionFormer*, an occlusion-aware framework based on DiT that explicitly models Z-order priority. It decouples the components first, then utilizes volumetric rendering for occlusion dependencies and a queried alignment loss for supervising individual instances and enhancing semantic consistency.
- Extensive experiments demonstrate that our method establishes a new state-of-the-art in the area of occlusion control, outperforming existing baselines in resolving complex occlusion and preserving semantic integrity.

2. Related Works

2.1. Layout-to-Image Generation

Training-free Methods. Training-free approaches (Xie et al., 2023; Bar-Tal et al., 2023; Li et al., 2025a) enforce spatial constraints at inference time by manipulating attention maps. LaRender (Zhan & Liu, 2025) further introduces volumetric rendering principles to simulate occlusion control. However, since these methods depend on heuristic gradients or latent edits instead of learned priors, they are often unstable and highly sensitive to hyperparameters. Thus, even with overlap handling, LaRender often fails to keep accurate spatial control in complex, multi-instance scenes.

Training-based Methods. Training-based methods inject stronger spatial guidance by adding trainable modules to diffusion backbones. Works based on U-Net such as GLIGEN (Li et al., 2023) and DiT-based models including EliGen (Zhang et al., 2025a) and Creatilayout (Zhang et al., 2025b) fuse box coordinates with visual features, typically improving fidelity and stability over training-free baselines. Nevertheless, they usually encode layout as a flattened 2D condition and overlook inter-object occlusion. Without an explicit occlusion-ordering mechanism, overlapping boxes yield ambiguous condition, causing feature entanglement where object appearances are unnaturally mixed.

2.2. Datasets for Layout-to-Image Generation

High-quality annotations are essential for training Layout-to-Image models with precise control. Early efforts used

Table 1. **Statistical comparison of datasets.** SA-Z features high-resolution, open-vocabulary, and 3D-aware annotations with rich geometric constraints compared to prior art. †: Resolution is classified as High if the image’s long edge > 1000px. ‡: SACap-1M derives captions from bounding box crops, where boxes often encompass irrelevant instances, this introduces visual noise into the generated texts.

Dataset	Source	#Image	#Instance	Resolution [†]	Vocabulary	Instance Caption	BBox	Mask	Z-order	Amodal
COCO 2017 (Lin et al., 2014)	COCO	≈ 0.1M	≈ 0.88M	Low	80	Class	✓	✓	×	×
InstaOrder (Lee & Park, 2022)	COCO	≈ 0.1M	≈ 0.50M	Low	80	Class	✓	✓	✓	×
COCOA (Zhu et al., 2017)	COCO	≈ 5.5K	≈ 69.0K	Low	80	Class	✓	✓	✓	✓
OpenImages (Kuznetsova et al., 2020)	Flickr	≈ 1.9M	≈ 16.0M	Vary	600	Class	✓	✓	×	×
Visual Genome (Krishna et al., 2017)	VG	≈ 0.1M	≈ 3.84M	Low	33,877	Phrase	✓	×	×	×
Eligen-Data (Zhang et al., 2025a)	Eligen	≈ 0.5M	≈ 1.26M	High	Open	Phrase	✓	×	×	×
LayoutSAM (Zhang et al., 2025b)	SA-1B	≈ 2.0M	≈ 10.7M	High	Open	Phrase	✓	×	×	×
SACap-1M (Li et al., 2025c)	SA-1B	≈ 1.0M	≈ 5.88M	High	Open	Phrase [‡]	✓	✓	×	×
SA-Z (Ours)	SA-1B	≈ 1.0M	≈ 5.69M	High	Open	Phrase	✓	✓	✓	✓

COCO (Lin et al., 2014) but were limited in scale. Recent datasets such as Eligen-Data (Zhang et al., 2025a), LayoutSAM (Zhang et al., 2025b), and SACap-1M (Li et al., 2025c) have significantly expanded data volume and annotation richness. However, they remain in 2D plane, overlooking Z-axis occlusion and invisible parts of objects that are vital for handling dense layouts. While specialized datasets like COCOA (Zhu et al., 2017) and InstaOrder (Lee & Park, 2022) provide Z-orders or amodal masks, they are inherently constrained by the low resolution and closed-set vocabulary of their underlying COCO images, rendering them unsuitable for modern open-vocabulary generation. To bridge this gap, we propose SA-Z, adapted from SACap-1M. We refine the dataset by generating pixel-level captions via DescribeAnything (Lian et al., 2025), predicting pairwise instance Z-orders with InstaOrderNet (Lee & Park, 2022), and estimating amodal annotations using SAM-3D (Chen et al., 2025). Detailed statistics of SA-Z are provided in Table 1.

3. Method

3.1. Preliminaries

Volume Rendering. Volumetric rendering (Mildenhall et al., 2020) is a differentiable mechanism that aggregates features along a ray \mathbf{r} via integral accumulation:

$$\hat{\mathbf{C}}(\mathbf{r}) = \sum_{i=1}^N T_i \alpha_i \mathbf{c}_i, \quad (1)$$

where \mathbf{c}_i is the feature at step i , and $\alpha_i = 1 - \exp(-\sigma_i)$ is opacity derived from density σ_i . $T_i = \exp(-\sum_{j=1}^{i-1} \sigma_j)$ denotes the transmittance, representing the probability of the ray remaining unblocked up to the step i .

Flow Matching. Flow Matching (Lipman et al., 2022) transports a source distribution p_0 (noise) to a target p_1 (data). Rectified Flow (Liu et al., 2022; Esser et al., 2024) adopts a linear interpolation path $\mathbf{z}_t = t\mathbf{x}_1 + (1-t)\mathbf{x}_0$. The model v_θ predicts the velocity $\mathbf{v}_{target} = \mathbf{x}_1 - \mathbf{x}_0$ by minimizing the following objective:

$$\mathcal{L}_{\text{flow}} = \mathbb{E}_{t, \mathbf{x}_0, \mathbf{x}_1} [\|v_\theta(\mathbf{z}_t, t) - (\mathbf{x}_1 - \mathbf{x}_0)\|_2^2]. \quad (2)$$

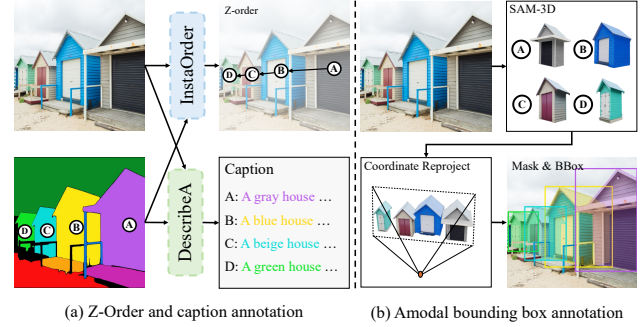


Figure 2. **Curation pipeline.** (a) Z-order and captions are annotated via InstaOrder and DescribeAnything. (b) Amodal BBoxes are derived by re-projecting 3D assets reconstructed by SAM-3D.

3.2. Dataset Curation

As shown in Figure 2, which illustrates the process with four instances for clarity, our curation pipeline augments the 2D masks of SACap-1M with three critical annotations to support occlusion-aware generation. First, to ensure semantic precision, we employ the pixel-level captioner DescribeAnything (Lian et al., 2025) to generate instance-specific descriptions strictly based on the mask area, avoiding visual noise from irrelevant adjacent instances. Second, to resolve occlusion ambiguity, we utilize InstaOrder (Lee & Park, 2022) to predict pairwise occlusion relationships, thereby establishing explicit Z-order information. Finally, to recover the full extent of occluded objects for facilitating occlusion supervision, we leverage SAM-3D (Chen et al., 2025) to lift instances into 3D space. By reconstructing the complete geometry and re-projecting it back to the image plane, we derive amodal mask and bounding boxes. As detailed in Table 1, SA-Z scales to 1M high-resolution images with 5.7M instances, uniquely featuring open-vocabulary amodal annotations. By incorporating the existing global prompt P from SACap-1M, we define each condition as a quintuple $(M_i, B_i, \mathcal{O}_i, C_i, P)$, representing the **Mask**, **Bounding box**, **Occluders**, instance **Caption**, and global **Prompt**.

3.3. OcclusionFormer

Extending Z-axis via Instance Decoupling. Previous methods like Eligen (Zhang et al., 2025a) and Creatilay-

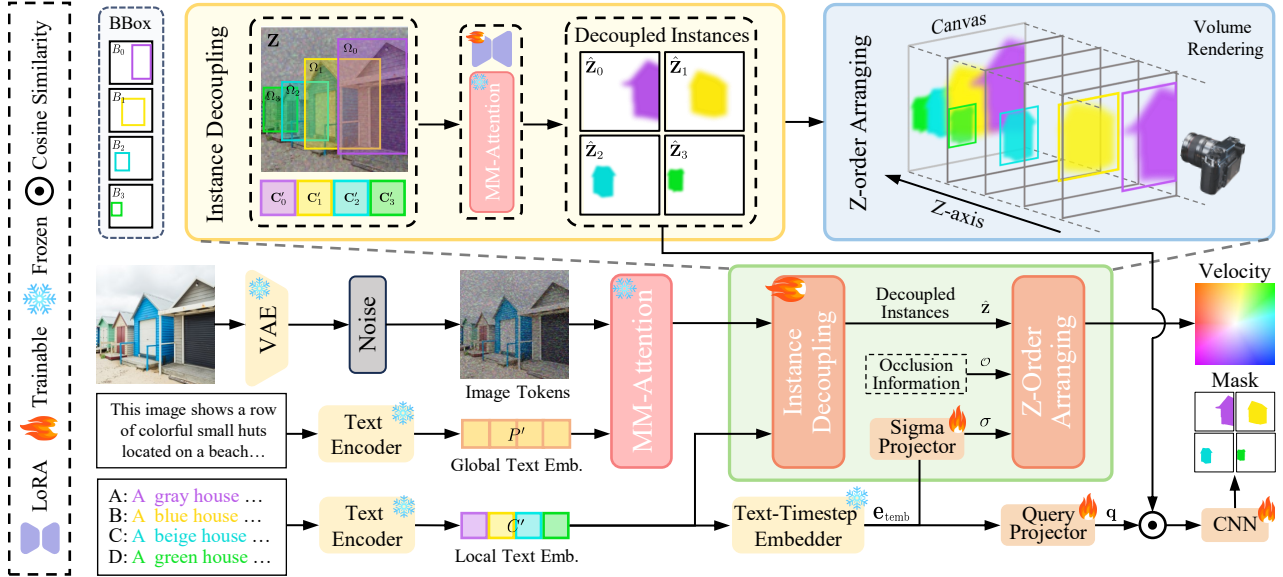


Figure 3. **The training pipeline of OcclusionFormer.** The framework decouples instances and recomposes them using volumetric rendering to resolve occlusions. Simultaneously, a queried alignment mechanism enforces strict spatial consistency via mask supervision.

out (Zhang et al., 2025b) control instance locations by injecting spatial information directly into the global Multi-Modal Attention (MM-Attention) (Esser et al., 2024). However, applying global attention across the entire 2D plane makes it difficult to explicitly model the order information across Z-axis, as all instances and background tokens interact indiscriminately. To address this, we propose extending the control into the Z-axis by decoupling instances into independent layers. As shown in Figure 3, our framework operates in a serial manner. Specifically, we derive the visual features $\mathbf{Z} \in \mathbb{R}^{L \times D}$ by processing the image tokens and the computed global prompt embedding P' through the preceding frozen MM-Attention block, where L is the sequence length and D denotes dimension. For each instance i , defined by its bounding box area B_i and caption C_i , we identify the subset of token indices Ω_i that fall within the region B_i :

$$\Omega_i = \{u \mid \text{Coord}(u) \in B_i\}, \quad (3)$$

where $\text{Coord}(u)$ maps a token index to its 2D spatial coordinates. Instead of attending to the global context, we extract the local visual sequence $\mathbf{Z}_{\Omega_i} \in \mathbb{R}^{|\Omega_i| \times D}$ corresponding to these indices. We then perform MM-Attention strictly between this local visual subset and the specific instance text embeddings C'_i calculated from instance caption C_i :

$$\hat{\mathbf{Z}}_{\Omega_i}, \hat{C}'_i = \text{MM-Attention}(\mathbf{Z}_{\Omega_i}, C'_i), \quad (4)$$

where $\text{MM-Attention}(\cdot, \cdot)$ represents the multi-modal attention reused from previous block and $\hat{\mathbf{Z}}_{\Omega_i}, \hat{C}'_i$ denote the updated features. We further assign that $\hat{\mathbf{Z}}_i$ equals $\hat{\mathbf{Z}}_{\Omega_i}$ within Ω_i and padding zero otherwise. To adapt the pre-trained backbone for instance control without compromising its original capability, we employ LoRA (Hu et al., 2022). We

freeze the original parameters and only optimize the injected LoRA layers within the attention projections. By calculating attention solely within the bounding box scope, we ensure that the visual features of instance i are modulated exclusively by its semantic description, effectively decoupling the generation of different instances before composing them.

Arranging the Z-order. To explicitly model the Z-order, we bring the idea of volume rendering from NeRF (Mildenhall et al., 2020). However, to adapt the principle of NeRF for the context of 2D image generation, we follow LaRender (Zhan & Liu, 2025) to view the image plane through a virtual orthogonal camera. We conceptualize the composition process as casting rays through the pixel space, arranged according to the provided set of occluder \mathcal{O} .

Drawing inspiration from the modulation vectors in Multi-modal Diffusion Transformers (Esser et al., 2024), we predict a learnable vector density $\sigma_i \in \mathbb{R}^D$ for each instance i , which is dynamically modulated based on the diffusion state for high-dimensional latent. Specifically, we first compute a conditioning embedding $\mathbf{e}_{\text{tomb}}^i$ for instance i by fusing the diffusion timestep t and pooled textual projections y_i from the text embedding C'_i via a time-text embedding module:

$$\mathbf{e}_{\text{tomb}}^i = \text{TimeTextEmbed}(t, y_i). \quad (5)$$

We then project this embedding $\mathbf{e}_{\text{tomb}}^i$ to obtain σ_i , effectively allowing the model to adaptively adjust the instance’s solidity according to different generation stages.

We then define the opacity $\alpha_i \in \mathbb{R}^D$ at pixel location \mathbf{p} as:

$$\alpha_i(\mathbf{p}) = (1 - \exp(-\sigma_i)) \cdot \mathbb{I}(\mathbf{p} \in B_i), \quad (6)$$

where $\mathbb{I}(\mathbf{p} \in B_i)$ acts as a binary spatial mask that restricts the instance’s opacity to be active only within its bounding

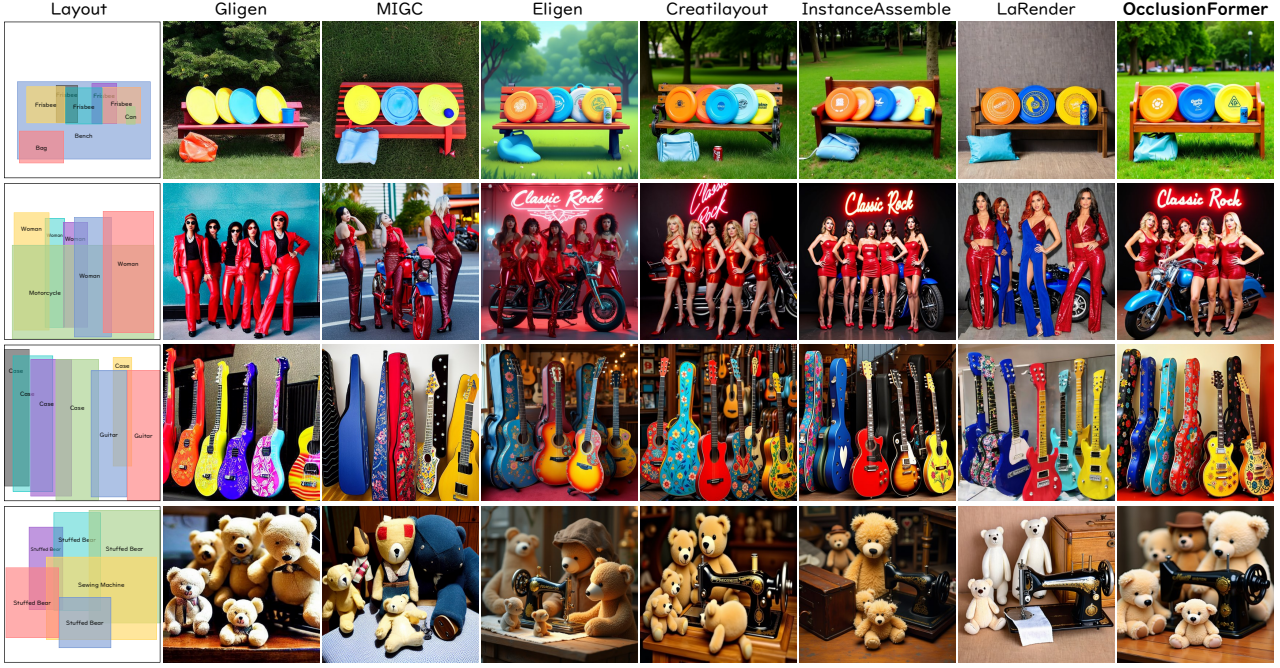


Figure 4. The visual comparison of different methods on the OverLayBench (Li et al., 2025b).

box B_i . To handle occlusion, we calculate the transmittance $T_i \in \mathbb{R}^D$, which denotes the probability of light reaching instance i without being blocked. Let \mathcal{O}_i be the set of occluders explicitly ordered in front of instance i . The transmittance is computed by element-wise operation as:

$$T_i(\mathbf{p}) = \exp\left(-\sum_{j \in \mathcal{O}_i} \sigma_j \cdot \mathbb{I}(\mathbf{p} \in B_j)\right). \quad (7)$$

This formulation ensures that if a dense occluder j covers the pixel, the transmittance T_i for the background object drops, effectively occluding the background object.

Finally, we define the rendering weight for instance i as $w_i(\mathbf{p}) = T_i(\mathbf{p}) \cdot \alpha_i(\mathbf{p})$. To ensure numerical stability and handle overlaps where no explicit occlusion relationship is defined between instances, we employ a hybrid aggregation strategy. For regions with valid occlusion weights, we perform a normalized weighted average. Otherwise, for overlapping regions without occlusion constraints (where only the boxes intersect but objects are non-overlapping), we default to a simple averaging of all features. The composed feature map $\mathbf{Z}_{out}(\mathbf{p})$ is computed as follows:

$$\mathbf{Z}_{out}(\mathbf{p}) = \begin{cases} \frac{\sum_i w_i(\mathbf{p}) \cdot \hat{\mathbf{Z}}_i(\mathbf{p})}{\sum_i w_i(\mathbf{p}) + \epsilon}, & \text{if } \sum_i w_i(\mathbf{p}) > 0 \\ \frac{1}{\max(1, |\mathcal{S}_p|)} \sum_{i \in \mathcal{S}_p} \hat{\mathbf{Z}}_i(\mathbf{p}), & \text{otherwise} \end{cases} \quad (8)$$

where \mathcal{S}_p is the set of bounding boxes of instances covering pixel \mathbf{p} , and ϵ is a small constant for stability. Finally, the input feature \mathbf{Z} is added to \mathbf{Z}_{out} via a residual connection.

Enhancing Alignment via Queried Loss. While volumetric rendering resolves occlusion ordering, it relies on the

premise that features form coherent geometric structures. To prevent spatial drift and enforce fine-grained shape consistency, we introduce a Queried Alignment Mechanism to explicitly supervise the spatial distribution of features.

For each instance i , we derive a learnable query vector $\mathbf{q}_i \in \mathbb{R}^D$ from the time-dependent embedding $\mathbf{e}_{i, \text{emb}}^i$. This query serves as a dynamic semantic anchor, intended to retrieve the spatial footprint of instance from the local visual features $\hat{\mathbf{Z}}_{\Omega_i}$ within $\hat{\mathbf{Z}}_i$. We first compute a spatial similarity map $\mathbf{S}_i \in \mathbb{R}^{H \times W}$ via pixel-wise cosine similarity:

$$\mathbf{S}_i(\mathbf{p}) = \frac{\hat{\mathbf{Z}}_i(\mathbf{p}) \cdot \mathbf{q}_i}{(\|\hat{\mathbf{Z}}_i(\mathbf{p})\| + \epsilon) \|\mathbf{q}_i\|}, \quad (9)$$

where ϵ is a small constant. To refine this coarse similarity into a precise shape, we feed \mathbf{S}_i into a lightweight CNN mask predictor \mathcal{F}_θ . The predictor outputs a probability map corresponding to background and foreground likelihoods:

$$\hat{\mathbf{M}}_i = \text{Softmax}(\mathcal{F}_\theta(\mathbf{S}_i)) \in [0, 1]^{H \times W \times 2}. \quad (10)$$

During training, we leverage masks M_i provided in SA-Z to enforce alignment via a Cross-Entropy loss \mathcal{L}_{align} , which encourages visual features to focus on valid object regions:

$$\mathcal{L}_{align} = -\frac{1}{N} \sum_{i, \mathbf{p}} \left[M_i \log(\hat{\mathbf{M}}_i^{fg}) + (1 - M_i) \log(\hat{\mathbf{M}}_i^{bg}) \right]. \quad (11)$$

Optimizing this queried loss forces the model to generate features $\hat{\mathbf{Z}}_{\Omega_i}$ that are not only semantically consistent but also aligned with the spatial geometry. As shown in Figure 6, the predicted foreground map $\hat{\mathbf{M}}_i^{fg}$ effectively captures the target geometry, validating the efficacy of our supervision.



Figure 5. The visual comparison of different methods on our constructed SA-Z Eval.

Training Objectives. The overall optimization objective combines generative capability with spatial alignment control. We train the model via a weighted sum:

$$\mathcal{L}_{\text{total}} = \mathcal{L}_{\text{flow}} + \lambda \cdot \mathcal{L}_{\text{align}}. \quad (12)$$

Here, $\mathcal{L}_{\text{flow}}$ follows the rectified flow matching formulation (Esser et al., 2024). Given the latent state \mathbf{z}_t at timestep t and conditions \mathbf{c} , the network v_θ learns to predict the ground-truth velocity $\mathbf{v}_{\text{target}}$:

$$\mathcal{L}_{\text{flow}} = \mathbb{E}_{t, \mathbf{z}_t, \mathbf{c}} [\|v_\theta(\mathbf{z}_t, t, \mathbf{c}) - \mathbf{v}_{\text{target}}\|_2^2]. \quad (13)$$

We empirically set the balancing coefficient $\lambda = 0.5$ to enforce sufficient geometry constraints without compromising the inherent visual quality of the pre-trained backbone.

4. Experiment

4.1. Experiment Settings

Our method is built upon Flux.1-dev (Labs, 2024) and compared against the previous U-Net-based (Li et al., 2023; Zhou et al., 2024; Zhan & Liu, 2025) and Flux-based (Zhang et al., 2025a;b; Xiang et al., 2025) baselines.

For evaluation, we utilize OverLayBench (Li et al., 2025b), as it specializes in assessing object occlusion and dense overlaps. To enable more detailed occlusion-aware evaluation, we additionally derive occlusion orders using SAM3 (Carion et al., 2025) and InstaOrder (Lee & Park, 2022). However, since OverLayBench consists of synthetic images generated by Flux, a domain gap inevitably exists with real-world

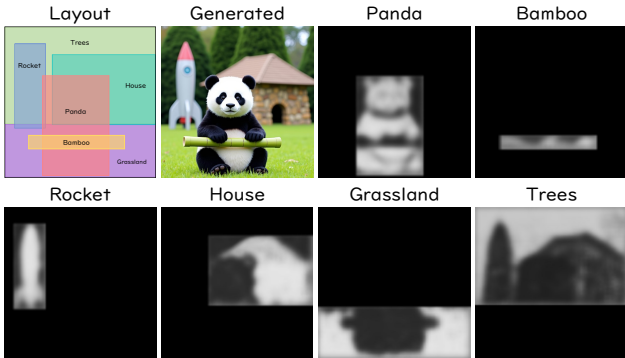


Figure 6. Visualization of the predicted foreground probability.

scenarios. To address this, we curate an additional SA-Z Eval with 1,000 images sampled from our SA-Z, specifically selecting cases with high instance counts and complex occlusion patterns to ensure rigorous realistic evaluation. These samples are excluded in training process. Following the protocols of OverLayBench, we report metrics across three dimensions: (1) Spatial Precision: We use mIoU for standard layout accuracy and O-mIoU to specifically evaluate intersection fidelity within complex overlapping regions. (2) Semantic Consistency: We employ VQA-based SR_E and SR_R using Qwen2.5-VL-32B (Bai et al., 2025) to verify entity existence and spatial relationship correctness, respectively. We also report Global (CLIP-G) and Local (CLIP-L) scores (Radford et al., 2021) for text-image alignment. (3) Image Quality: FID (Heusel et al., 2017) is included to assess the realism of generated images. Additionally, based on the derived occlusion annotations, we report occlusion-aware metrics used in InstaOrder: Occ. (Occlusion Order,

Table 2. Comparison results on Simple, Regular, and Complex subsets on OverLayBench (Li et al., 2025b) and SA-Z Eval.

Subset	Method	mIoU \uparrow	O-mIoU \uparrow	SR $_E\uparrow$	SR $_R\uparrow$	CLIP-G \uparrow	CLIP-L \uparrow	FID \downarrow	Occ. \uparrow	Dep. \downarrow
OverLay-Simple	GLIGEN	0.6380	0.3847	0.4885	0.7849	0.3243	0.2473	36.732	0.6055	0.2414
	MIGC	0.6009	0.3350	0.6340	0.8044	0.3260	0.2683	33.382	0.5631	0.2607
	LaRender	0.6604	0.4136	0.5665	0.7767	0.2882	0.2608	38.674	0.6294	0.2378
	Eligen	0.6673	0.4151	0.8813	<u>0.9165</u>	0.3654	0.2865	27.908	0.6823	0.2118
	Creatilayout	0.6998	0.4725	0.8255	0.9094	0.3737	0.2827	25.026	0.7559	0.1792
	InstanceAssemble	<u>0.7279</u>	<u>0.5152</u>	<u>0.9043</u>	0.9105	0.3664	<u>0.2882</u>	<u>24.768</u>	<u>0.7852</u>	<u>0.1621</u>
	OcclusionFormer	0.7405	0.5456	0.9241	0.9257	<u>0.3711</u>	0.2896	24.596	0.8051	0.1559
OverLay-Regular	GLIGEN	0.5549	0.2960	0.4577	0.7701	0.3232	0.2346	58.122	0.5831	0.2431
	MIGC	0.4836	0.2069	0.5663	0.7752	0.3208	0.2530	57.290	0.4569	0.2660
	LaRender	0.5721	0.3006	0.5497	0.7540	0.2867	0.2607	60.935	0.5862	0.2305
	Eligen	0.5680	0.3075	0.8437	0.8727	0.3624	0.2712	44.839	0.6186	0.2076
	Creatilayout	0.5997	0.3517	0.7523	0.8604	<u>0.3633</u>	0.2648	43.368	0.7124	0.1765
	InstanceAssemble	<u>0.6299</u>	<u>0.3861</u>	<u>0.8795</u>	<u>0.8746</u>	0.3625	<u>0.2725</u>	43.068	<u>0.7475</u>	<u>0.1659</u>
	OcclusionFormer	0.6487	0.4161	0.8822	0.8821	0.3639	0.2745	42.712	0.7811	0.1575
OverLay-Complex	GLIGEN	0.5468	0.2763	0.4018	0.8046	0.3219	0.2290	62.647	0.5951	0.2251
	MIGC	0.4024	0.1367	0.4863	0.7487	0.3132	0.2470	69.397	0.4091	0.2968
	LaRender	0.5227	0.2507	0.4508	0.7462	0.2685	0.2473	67.884	0.6026	0.2374
	Eligen	0.5195	0.2569	0.7988	<u>0.8794</u>	0.3604	0.2582	49.421	0.5994	0.2378
	Creatilayout	0.5584	0.3006	0.6923	<u>0.8750</u>	<u>0.3622</u>	0.2532	47.793	<u>0.7142</u>	0.1907
	InstanceAssemble	<u>0.5706</u>	<u>0.3189</u>	<u>0.8348</u>	0.8761	0.3608	0.2658	<u>46.673</u>	0.6987	<u>0.1791</u>
	OcclusionFormer	0.6037	0.3468	0.8531	0.8890	0.3648	<u>0.2640</u>	46.166	0.7797	0.1602
SA-Z Eval	GLIGEN	0.3837	0.1695	0.7180	0.7437	0.3074	0.2093	75.134	0.6778	0.1805
	MIGC	0.3076	0.0958	0.6375	0.7313	0.3003	0.2270	73.443	0.6191	0.2531
	LaRender	0.4053	0.1709	0.7128	0.7449	0.2673	0.2293	77.983	0.6833	0.1790
	Eligen	0.3007	0.1016	0.8056	0.8525	0.3487	0.2385	69.910	0.6095	0.2533
	Creatilayout	0.4216	0.1904	<u>0.8129</u>	0.8575	0.3501	<u>0.2446</u>	64.659	0.6921	0.1837
	InstanceAssemble	<u>0.4292</u>	<u>0.2021</u>	0.8074	0.8421	0.3512	0.2439	63.654	0.6947	0.1711
	OcclusionFormer	0.4509	0.2231	0.8158	<u>0.8527</u>	0.3514	0.2466	62.786	0.7568	0.1529

measured by F1 score) and Dep. (Depth Order, measured by WHDR (Bell et al., 2014)), which quantifies the disagreement between predicted and ground truth depth layers. For implementation, we set LoRA rank to 4 and train for 200K steps with a batch size of 16 and a learning rate of $1e^{-4}$.

4.2. Experiment Results

We present the quantitative comparisons on the OverLayBench benchmark (Li et al., 2025b) and SA-Z Eval in Table 2. The evaluation is conducted across Simple, Regular, Complex subsets and SA-Z Eval to assess model performance under varying degrees of spatial intricacy. To derive the occlusion and depth annotations for evaluation, we first utilize SAM3 (Carion et al., 2025) to segment the generated distinct instances. Subsequently, these segmented instances are fed into the InstaOrderNet and InstaDepthNet modules within the InstaOrder framework (Lee & Park, 2022) to predict the occlusion order and depth order, respectively.

Qualitative Analysis. Visual comparisons on OverLayBench and SA-Z Eval are presented in Figure 4 and Figure 5, respectively, which reveal that baselines often suffer from object fusion or incorrect Z-order in dense overlap scenes. In contrast, by explicitly modeling Z-axis priority, OcclusionFormer generates distinct instances with correct occlusion dependencies, maintaining structural integrity.



Figure 7. Ablation study of different settings of OcclusionFormer.

Z-axis Consistency and Occlusion Handling. Our method establishes a new state-of-the-art in occlusion-aware metrics (O-mIoU, Occ., Dep.) across both the OverLayBench and our curated SA-Z Eval. This decisive advantage stems from our explicit Z-order modeling via Volumetric Rendering, rather than implicit global attention. By calculating the transmittance T_i derived from the predicted density of occluders, our mechanism effectively suppresses background features in overlapping regions while preserving foreground visibility. This dynamic opacity modulation ensures instances are rendered strictly according to the Z-order, yielding Occ. scores of 0.7797 (Complex) and 0.7568 (SA-Z

Table 3. Ablation study on the Complex subset of OverLayBench (Li et al., 2025b) and our created SA-Z Eval. We analyze the impact of dynamic density, queried alignment losses, and occlusion conditioning, highlighting the contribution of each component.

Subset	Method	mIoU \uparrow	O-mIoU \uparrow	SR $_E\uparrow$	SR $_R\uparrow$	CLIP-G \uparrow	CLIP-L \uparrow	FID \downarrow	Occ. \uparrow	Dep. \downarrow
OverLay-Complex	w/o Learned Sigma	0.5911	0.3276	0.8482	0.8781	0.3624	0.2617	46.258	0.7530	0.1694
	w/o Queried Loss	0.5922	0.3319	0.8436	0.8798	0.3613	0.2611	46.094	0.7659	0.1666
	w Attn. Map Loss	0.5753	0.3207	0.8353	0.8773	0.3599	0.2602	46.433	0.7510	0.1695
	w/o Amodal Data	0.6004	0.3411	0.8496	0.8855	0.3617	0.2621	46.265	0.7703	0.1644
	w/o Inst. Decouple	0.5177	0.2786	0.8043	0.8768	0.3610	0.2569	47.734	0.6109	0.2310
	w/o Occlusion Cond.	0.5912	0.3294	0.8505	0.8800	0.3611	0.2623	46.358	0.7262	0.1739
	OcclusionFormer		0.6037	0.3468	0.8531	0.8890	0.3648	0.2640	46.166	0.7797
SA-Z Eval	w/o Learned Sigma	0.4407	0.2133	0.8084	0.8460	0.3523	0.2445	63.233	0.7358	0.1586
	w/o Queried Loss	0.4459	0.2211	0.8024	0.8432	0.3480	0.2436	63.213	0.7444	0.1625
	w Attn. Map Loss	0.4250	0.2013	0.8128	0.8376	0.3512	0.2405	64.125	0.7359	0.1700
	w/o Amodal Data	0.4462	0.2191	0.8064	0.8462	0.3492	0.2453	62.821	0.7491	0.1556
	w/o Inst. Decouple	0.3409	0.1350	0.7645	0.8201	0.3465	0.2295	66.576	0.6393	0.2480
	w/o Occlusion Cond.	0.4417	0.2151	0.8107	0.8503	0.3486	0.2471	63.505	0.7188	0.1676
	OcclusionFormer		0.4509	0.2231	0.8158	0.8527	0.3514	0.2466	62.786	0.7568

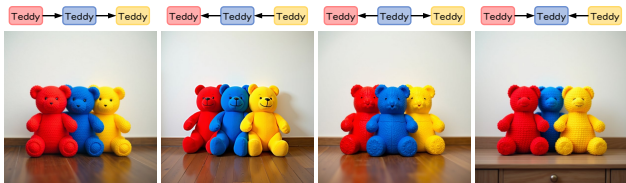


Figure 8. Limitations of OcclusionFormer. Arrows indicate the direction of occlusion. Best viewed when zoomed in.

Eval), demonstrating robustness in challenging scenarios.

Spatial Precision and Semantic Alignment. Beyond occlusion, our framework excels in 2D layout accuracy and semantic identity, achieving the highest mIoU and O-mIoU scores. We attribute this to the synergy between Instance Decoupling and the Queried Alignment Mechanism. Decoupling the attention computation into local subsets prevents feature bleeding from background tokens. Furthermore, the Queried Alignment loss \mathcal{L}_{align} forces these features to conform to geometry shapes. This filters out noise outside the valid object boundaries, thereby enhancing both the boundary precision and the purity of semantic features (CLIP/SR).

4.3. Ablation Study

To validate the effectiveness of OcclusionFormer, we conduct ablation studies on both OverLayBench-Complex and SA-Z Eval in Table 3, and the full results are provided in the appendix. Visual examples are presented in Figure 7.

Significance of Instance Decoupling. Reverting to global attention (*w/o Inst. Decouple*) causes the most severe performance collapse across both subsets. The consistent drop in mIoU and Occ. metrics confirms that decoupling is fundamental to prevent feature entanglement between overlapping instances and background tokens, regardless of the domain.

Z-order Modeling and Consistency. Removing explicit Z-order (*w/o Occlusion Cond.*) lowers occlusion accuracy on both benchmarks, proving 2D boxes are insufficient for

complex overlaps. Similarly, employing a fixed scalar density (specifically, setting $\sigma = 5$ in *w/o Learned Sigma*) consistently degrades performance, validating that opacity should be dynamically modulated across diffusion steps to coordinate the transition from noise to structure.

Spatial Alignment and Amodal Data. Removing the auxiliary loss (*w/o Queried Loss*) drops O-mIoU, while using a naive BCE loss on the attention map (*w Attn. Map Loss*) further harms performance across datasets, confirming the necessity of our queried loss. Additionally, training without amodal annotations (*w/o Amodal Data*) yields suboptimal results in both settings, indicating that full amodal shapes provide vital geometric signals for learning occlusion.

5. Conclusion

To address the challenge of inter-object occlusion in layout-to-image generation, we introduce **SA-Z**, a large-scale dataset enriched with explicit Z-order annotations. Building on this, we propose **OcclusionFormer**, an occlusion-aware framework that models the Z-order via volumetric rendering to resolve the order ambiguities in Z-axis and queried alignment to ensure spatial precision. Extensive evaluations on the benchmarks demonstrate that OcclusionFormer establishes a new state-of-the-art, significantly outperforming baselines in both occlusion accuracy and visual fidelity.

Limitations & Future Work. As illustrated in Figure 8, we generate images using identical layouts and seeds, varying only the occlusion order. While the Z-order arrangement shifts correctly, we observe noticeable inconsistencies in object identity (e.g., variations in the texture and details of the teddy bear). This suggests that the appearance is not fully disentangled from occlusion order. Despite this limitation, our method serves as a foundational baseline for occlusion-aware generation, and we envision that future work could further enhance precision and consistency by incorporating post-training strategies, such as Reinforcement Learning.

Impact Statement

This paper presents *OcclusionFormer*, which improves layout-to-image generation through explicit Z-order control. While the model shares standard risks associated with generative AI, such as inheriting biases from the pre-trained backbone or potential misuse, it significantly enhances structural fidelity in dense overlapped scenes. This capability offers practical benefits for creative design workflows and the generation of high-quality synthetic training data.

References

- Bai, S., Chen, K., Liu, X., Wang, J., Ge, W., Song, S., Dang, K., Wang, P., Wang, S., Tang, J., et al. Qwen2. 5-vl technical report. *arXiv*, 2025.
- Bar-Tal, O., Yariv, L., Lipman, Y., and Dekel, T. Multi-diffusion: Fusing diffusion paths for controlled image generation. *arXiv*, 2023.
- Bell, S., Bala, K., and Snavely, N. Intrinsic images in the wild. *ACM TOG*, 2014.
- Carion, N., Gustafson, L., Hu, Y.-T., Debnath, S. F., Hu, R., Suris, D., Ryali, C., Alwala, K. V., Khedr, H., Huang, A., et al. Sam 3: Segment anything with concepts. *arXiv*, 2025.
- Chen, X., Chu, F.-J., Gleize, P., Liang, K. J., Sax, A., Tang, H., Wang, W., Guo, M., Hardin, T., Li, X., et al. Sam 3d: 3dfy anything in images. *arXiv*, 2025.
- Chen, Z., Li, Y., Wang, H., Chen, Z., Jiang, Z., Li, J., Wang, Q., Yang, J., and Tai, Y. Region-aware text-to-image generation via hard binding and soft refinement. *arXiv*, 2024.
- Cheng, B., Ma, Y., Wu, L., Liu, S., Ma, A., Wu, X., Leng, D., and Yin, Y. Hico: Hierarchical controllable diffusion model for layout-to-image generation. In *NeurIPS*, 2024.
- Esser, P., Kulal, S., Blattmann, A., Entezari, R., Müller, J., Saini, H., Levi, Y., Lorenz, D., Sauer, A., Boesel, F., et al. Scaling rectified flow transformers for high-resolution image synthesis. In *ICML*, 2024.
- He, R., Cheng, B., et al. Plangen: Towards unified layout planning and image generation in auto-regressive vision language models. In *ICCV*, 2025.
- Heusel, M., Ramsauer, H., Unterthiner, T., Nessler, B., and Hochreiter, S. Gans trained by a two time-scale update rule converge to a local nash equilibrium. In *NeurIPS*, 2017.
- Hu, E. J., Shen, Y., Wallis, P., Allen-Zhu, Z., Li, Y., Wang, S., Wang, L., Chen, W., et al. Lora: Low-rank adaptation of large language models. In *ICLR*, 2022.
- Kirillov, A., Mintun, E., Ravi, N., Mao, H., Rolland, C., Gustafson, L., Xiao, T., Whitehead, S., Berg, A. C., Lo, W.-Y., et al. Segment anything. In *ICCV*, 2023.
- Krishna, R., Zhu, Y., Groth, O., Johnson, J., Hata, K., Kravitz, J., Chen, S., Kalantidis, Y., Li, L.-J., Shamma, D. A., et al. Visual genome: Connecting language and vision using crowdsourced dense image annotations. *IJCV*, 2017.
- Kuznetsova, A., Rom, H., Alldrin, N., Uijlings, J., Krasin, I., Pont-Tuset, J., Kamali, S., Popov, S., Mallocci, M., Kolesnikov, A., et al. The open images dataset v4: Unified image classification, object detection, and visual relationship detection at scale. *IJCV*, 2020.
- Labs, B. F. Flux.1-dev, 2024.
- Lee, H. and Park, J. Instance-wise occlusion and depth orders in natural scenes. In *CVPR*, 2022.
- Li, B., Hu, Y., Liu, S., and Wang, X. Control and realism: Best of both worlds in layout-to-image without training. In *ICML*, 2025a.
- Li, B., Wang, C.-Y., Xu, H., Zhang, X., Armand, E., Srivastava, D., Shan, X., Chen, Z., Xie, J., and Tu, Z. Overlay-bench: A benchmark for layout-to-image generation with dense overlaps. In *NeurIPS*, 2025b.
- Li, D., Zhang, H., Wang, S., Li, J., and Wu, Z. Seg2any: Open-set segmentation-mask-to-image generation with precise shape and semantic control. In *NeurIPS*, 2025c.
- Li, Y., Liu, H., Wu, Q., Mu, F., Yang, J., Gao, J., Li, C., and Lee, Y. J. Gligen: Open-set grounded text-to-image generation. In *CVPR*, 2023.
- Li, Z., Luo, H., Shuai, X., and Ding, H. Anyi2v: Animating any conditional image with motion control. In *ICCV*, 2025d.
- Lian, L., Ding, Y., Ge, Y., Liu, S., Mao, H., Li, B., Pavone, M., Liu, M.-Y., Darrell, T., Yala, A., et al. Describe anything: Detailed localized image and video captioning. In *ICCV*, 2025.
- Lin, K. H., Mo, S., Klingher, B., Mu, F., and Zhou, B. Ctrl-x: Controlling structure and appearance for text-to-image generation without guidance. In *NeurIPS*, 2024.
- Lin, T.-Y., Maire, M., Belongie, S., Hays, J., Perona, P., Ramanan, D., Dollár, P., and Zitnick, C. L. Microsoft coco: Common objects in context. In *ECCV*, 2014.
- Lipman, Y., Chen, R. T., Ben-Hamu, H., Nickel, M., and Le, M. Flow matching for generative modeling. *arXiv*, 2022.

- Liu, X., Gong, C., and Liu, Q. Flow straight and fast: Learning to generate and transfer data with rectified flow. In *NeurIPS*, 2022.
- Lv, Z., Wei, Y., Zuo, W., and Wong, K.-Y. K. Place: Adaptive layout-semantic fusion for semantic image synthesis. In *CVPR*, 2024.
- Mildenhall, B., Srinivasan, P. P., Tancik, M., Barron, J. T., Ramamoorthi, R., and Ng, R. Nerf: Representing scenes as neural radiance fields for view synthesis. In *ECCV*, 2020.
- Mo, S., Mu, F., Lin, K. H., Liu, Y., Guan, B., Li, Y., and Zhou, B. Freecontrol: Training-free spatial control of any text-to-image diffusion model with any condition. In *CVPR*, 2024.
- Qin, Z., Shuai, X., and Ding, H. Scenedesigner: Controllable multi-object image generation with 9-dof pose manipulation. In *NeurIPS*, 2025.
- Radford, A., Kim, J. W., Hallacy, C., Ramesh, A., Goh, G., Agarwal, S., Sastry, G., Askell, A., Mishkin, P., Clark, J., et al. Learning transferable visual models from natural language supervision. In *ICML*, 2021.
- Sun, Y., Liu, Y., Tang, Y., Pei, W., and Chen, K. Any-control: create your artwork with versatile control on text-to-image generation. In *ECCV*, 2024.
- Wang, X., Darrell, T., Rambhatla, S. S., Girdhar, R., and Misra, I. Instancediffusion: Instance-level control for image generation. In *CVPR*, 2024.
- Xiang, Q., Sun, S., Li, B., Song, D., Li, H., Chen, N., Tang, X., Hu, Y., and Zhang, J. Instanceassemble: Layout-aware image generation via instance assembling attention. In *NeurIPS*, 2025.
- Xie, J., Li, Y., Huang, Y., Liu, H., Zhang, W., Zheng, Y., and Shou, M. Z. Boxdiff: Text-to-image synthesis with training-free box-constrained diffusion. In *ICCV*, 2023.
- Zhan, X. and Liu, D. Larender: Training-free occlusion control in image generation via latent rendering. In *ICCV*, 2025.
- Zhang, H., Duan, Z., Wang, X., Chen, Y., and Zhang, Y. Eligen: Entity-level controlled image generation with regional attention. *arXiv*, 2025a.
- Zhang, H., Hong, D., Wang, Y., Shao, J., Wu, X., Wu, Z., and Jiang, Y.-G. Creatilayout: Siamese multimodal diffusion transformer for creative layout-to-image generation. In *ICCV*, 2025b.
- Zhang, L., Rao, A., and Agrawala, M. Adding conditional control to text-to-image diffusion models. In *ICCV*, 2023.
- Zhou, D., Li, Y., Ma, F., Zhang, X., and Yang, Y. Migc: Multi-instance generation controller for text-to-image synthesis. In *CVPR*, 2024.
- Zhu, Y., Tian, Y., Metaxas, D., and Dollár, P. Semantic amodal segmentation. In *CVPR*, 2017.

Appendix for: OcclusionFormer: Arranging Z-Order for Layout-Grounded Image Generation

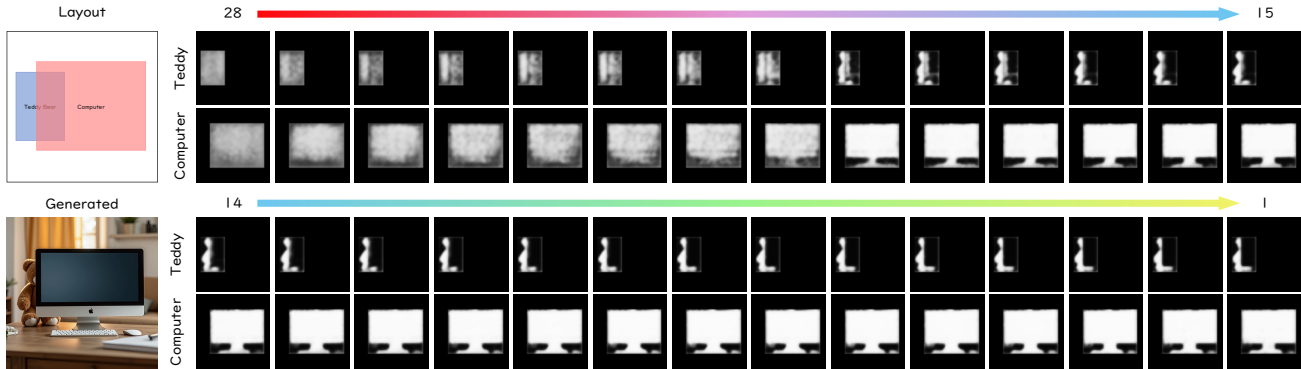


Figure 9. Progression of predicted masks during the denoising process, with the total number of timesteps set to 28.

A. More Implementation Details

Conditioning Projections and Softplus Activation. To derive instance-specific control parameters, we employ an adaptive projection module. This module processes the time-dependent text embedding through a SiLU activation followed by two parallel Linear layers. One Linear layer projects the semantic query vector \mathbf{q}_i to retrieve spatial alignment features via cosine similarity. The other Linear layer predicts the raw density value for the instance. To strictly enforce the physical constraint that optical density must be non-negative, we apply the Softplus activation function to the raw output of the density projection layer:

$$\sigma_i = \text{Softplus}(\text{Linear}(\text{SiLU}(\mathbf{e}_{\text{temb}}))). \quad (14)$$

Mask Predictor Architecture. The mask predictor, designed to refine the coarse spatial similarity map into precise foreground-background probability, is implemented as a lightweight Convolutional Neural Network (CNN). It takes a single-channel similarity map as input and processes it through the following structure:

1. A 3×3 convolution ($1 \rightarrow 32$ channels, padding 1) followed by GELU activation;
2. A 3×3 convolution ($32 \rightarrow 16$ channels, padding 1) followed by GELU activation;
3. A 1×1 convolution ($16 \rightarrow 2$ channels) to output the logits for background and foreground probabilities.

Training and Inference Strategy. During training, we adopt a time-dependent mask supervision strategy. Specifically, we utilize amodal masks as the supervision target during high noise levels (e.g., $t \in [700, 1000]$) to establish

global structure, and switch to modal (visible) masks for the remaining steps (e.g., $t < 700$). This curriculum encourages the model to reconstruct complete amodal features in the early phase to facilitate occlusion learning, while prioritizing precise visible boundary refinement in the later stages. During inference, we employ a 28-step denoising schedule. Following foundation work (Li et al., 2023), layout guidance is activated exclusively during the initial 30% of the denoising process for the balance of quality and speed. All our experiments are implemented on Nvidia A800 GPUs.

B. Investigation of Predicted Masks

As visualized in Figure 9, we investigate the evolution of the predicted foreground probability maps \hat{M}_i^{fg} predicted by mask predictor in the location of the first single-stream block throughout the denoising process. At the early stages, the mask predictor focuses on capturing the coarse and amodal spatial footprint of the instances, roughly filling the entire bounding box area. However, as the denoising progresses toward the final steps, the masks gradually become sharper and conform to the fine-grained object boundaries.

C. More Qualitative Comparison

We provide additional visual comparisons to further substantiate the qualitative superiority of the proposed OcclusionFormer over existing state-of-the-art methods. We provide additional visual comparisons to evaluate the generation quality. Figure 10 presents results on OverLayBench (Li et al., 2025b), demonstrating our method’s superiority in handling dense overlaps and preserving instance boundaries compared to previous methods. Figure 11 showcases the performance on our SA-Z Eval benchmark, verifying that our approach consistently maintains high realism and structural fidelity even in complex real-world scenarios.

Table 4. Full ablation study on the Simple, Regular, Complex subsets of OverLayBench (Li et al., 2025b) and our SA-Z Eval.

Subset	Method	mIoU \uparrow	O-mIoU \uparrow	SR $_E\uparrow$	SR $_R\uparrow$	CLIP-G \uparrow	CLIP-L \uparrow	FID \downarrow	Occ. \uparrow	Dep. \downarrow
OverLay-Simple	Flux.1-dev	0.3958	0.1937	0.7878	0.8959	0.3746	0.2475	24.282	0.5378	0.2586
	w/o Learned Sigma	0.7346	0.5391	0.9182	0.9287	0.3673	0.2895	24.716	0.7883	0.1588
	w/o Queried Loss	0.7390	0.5347	0.9130	0.9283	0.3674	0.2889	24.763	0.7919	0.1624
	w Attn. Map Loss	0.7196	0.5042	0.9096	0.9188	0.3665	0.2875	24.880	0.7833	0.1681
	w/o Amodal Data	0.7368	0.5460	0.9234	0.9268	0.3703	0.2880	24.630	0.8013	0.1583
	w/o Inst. Decouple	0.6844	0.4879	0.8975	0.9142	0.3682	0.2830	25.264	0.7050	0.1954
	w/o Occlusion Cond.	0.7385	0.5405	0.9235	0.9204	0.3659	0.2885	24.796	0.7822	0.1606
	OcclusionFormer	0.7405	0.5456	0.9241	0.9257	0.3711	0.2896	24.596	0.8051	0.1559
OverLay-Regular	Flux.1-dev	0.3250	0.1410	0.7223	0.8434	0.3704	0.2327	43.670	0.5081	0.2562
	w/o Learned Sigma	0.6321	0.4046	0.8767	0.8819	0.3626	0.2742	42.881	0.7542	0.1591
	w/o Queried Loss	0.6367	0.4098	0.8714	0.8761	0.3630	0.2738	42.779	0.7629	0.1599
	w Attn. Map Loss	0.6150	0.3866	0.8689	0.8727	0.3609	0.2724	43.198	0.7536	0.1594
	w/o Amodal Data	0.6454	0.4132	0.8798	0.8803	0.3644	0.2744	42.679	0.7793	0.1623
	w/o Inst. Decouple	0.5843	0.3456	0.8573	0.8718	0.3605	0.2675	45.668	0.6728	0.2334
	w/o Occlusion Cond.	0.6301	0.4028	0.8824	0.8801	0.3616	0.2750	43.412	0.7691	0.1586
	OcclusionFormer	0.6487	0.4161	0.8822	0.8821	0.3639	0.2745	42.712	0.7811	0.1575
OverLay-Complex	Flux.1-dev	0.3342	0.1402	0.6345	0.8695	0.3706	0.2276	46.609	0.4611	0.2846
	w/o Learned Sigma	0.5911	0.3276	0.8482	0.8781	0.3624	0.2617	46.258	0.7530	0.1694
	w/o Queried Loss	0.5922	0.3319	0.8436	0.8798	0.3613	0.2611	46.094	0.7659	0.1666
	w Attn. Map Loss	0.5753	0.3207	0.8353	0.8773	0.3599	0.2602	46.433	0.7510	0.1695
	w/o Amodal Data	0.6004	0.3411	0.8496	0.8855	0.3617	0.2621	46.265	0.7703	0.1644
	w/o Inst. Decouple	0.5177	0.2786	0.8043	0.8768	0.3610	0.2569	47.734	0.6109	0.2310
	w/o Occlusion Cond.	0.5912	0.3294	0.8505	0.8800	0.3611	0.2623	46.358	0.7262	0.1739
	OcclusionFormer	0.6037	0.3468	0.8531	0.8890	0.3648	0.2640	46.166	0.7797	0.1602
SA-Z Eval	Flux.1-dev	0.1887	0.0536	0.7845	0.8202	0.3525	0.2127	70.226	0.4269	0.2944
	w/o Learned Sigma	0.4407	0.2133	0.8084	0.8460	0.3523	0.2445	63.233	0.7358	0.1586
	w/o Queried Loss	0.4459	0.2211	0.8024	0.8432	0.3480	0.2436	63.213	0.7444	0.1625
	w Attn. Map Loss	0.4250	0.2013	0.8128	0.8376	0.3512	0.2405	64.125	0.7359	0.1700
	w/o Amodal Data	0.4462	0.2191	0.8064	0.8462	0.3492	0.2453	62.821	0.7491	0.1556
	w/o Inst. Decouple	0.3409	0.1350	0.7645	0.8201	0.3465	0.2295	66.576	0.6393	0.2480
	w/o Occlusion Cond.	0.4417	0.2151	0.8107	0.8503	0.3486	0.2471	63.505	0.7188	0.1676
	OcclusionFormer	0.4509	0.2231	0.8158	0.8527	0.3514	0.2466	62.786	0.7568	0.1529

D. More Ablation Results

Table 4 details the full ablation study across OverLayBench and SA-Z Eval. We include Flux.1-dev to establish a lower bound for spatial metrics (e.g., mIoU, O-mIoU, Occ., Dep.). Notably, Flux achieves high CLIP-G scores due to direct derivation from global prompts. Regarding fidelity, Flux naturally exhibits low FID on OverLayBench as the dataset itself is synthesized by Flux. However, its FID performance degrades on the real-world SA-Z Eval. Beyond this baseline, we observe distinct trends regarding specific components.

First, removing instance decoupling (*w/o Inst. Decouple*) results in the most severe degradation. For instance, in the Complex subset, mIoU drops significantly from 0.6037 to 0.5177, and Occlusion accuracy (Occ.) falls from 0.7797 to 0.6109. This confirms that decoupling is foundational, essential for preventing feature entanglement and ensuring individual instances are generated with distinct identities.

Second, the significance of explicit Z-order modeling (*w/o Occlusion Cond.*) exhibits a clear correlation with scene complexity. On the Simple subset where overlaps are min-

imal, the model performs comparably to the full method (mIoU 0.7385 vs. 0.7405). However, on Complex subsets and SA-Z Eval featuring dense and intricate overlaps, the lack of explicit Z-order leads to a notable drop in performance (e.g., Occ. drops roughly 5.3% on Complex). This demonstrates that while implicit learning suffices for simple layouts, explicit volumetric rendering is indispensable for resolving intricate occlusion relationships.

Third, regarding the spatial alignment components, both *Learned Sigma* and *Queried Loss* prove critical for fine-grained spatial precision. Removing the learned density (*w/o Learned Sigma*) harms the ability to modulate opacity dynamically, leading to a decreased O-mIoU. Similarly, removing the alignment loss (*w/o Queried Loss*) compromises boundary precision, evidenced by the decline in SR $_E$ across all sets (e.g., 0.8158 to 0.8024 on SA-Z Eval).

Finally, training without amodal annotations (*w/o Amodal Data*) fails to maintain the structural integrity of occluded objects. While achieving competitive FID scores, the degradation in O-mIoU, Occlusion Order (Occ.), and Depth Order (Dep.) across Complex subsets and SA-Z Eval highlights

Table 5. User study results comparing Occ., Layout Align, Local Fidelity, and Global Align, the higher is better.

Method	Occ.↑	Layout Align ↑	Local Fidelity↑	Global Align↑
GLIGEN	0.5486	0.6257	0.4838	0.5152
MIGC	0.2086	0.1790	0.1676	0.3657
LaRender	0.5838	0.5433	0.4824	0.2314
Eligen	0.5390	0.5776	0.5543	0.6876
Creatilayout	<u>0.6743</u>	0.6567	0.7295	0.7095
InstanceAssemble	0.6424	<u>0.6919</u>	<u>0.7738</u>	<u>0.7390</u>
Ours	0.7833	0.7357	0.8086	0.7514

that amodal supervision provides vital geometric signals for learning correct occlusion dependencies.

E. User Study

We conducted a user study employed 15 participants with 300 randomly selected samples from the OverLayBench *Complex* subset and our constructed *SA-Z Eval* benchmark. Evaluators ranked the images of 7 methods based on occlusion accuracy, layout alignment, local fidelity, and global alignment. Scores were assigned from 1 to 7 based on the ranking and normalized to $[1/7, 1]$. As reported in Table 5, our method achieves the highest ratings across all four dimensions, confirming its superiority in human perceptual evaluation over existing state-of-the-art baselines.

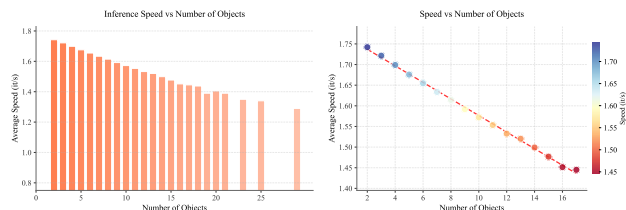


Figure 12. **Efficiency analysis.** We report the inference speed on NVIDIA A800 GPU with varying numbers of objects. The results show a linear scaling trend, ensuring efficiency in dense scenes.

F. Efficiency Analysis

We investigate the computational efficiency of our proposed framework by evaluating the inference speed on a single NVIDIA A800 GPU. Given that our method employs an instance decoupling strategy to process local features, the computational cost is correlated with the scene complexity. As illustrated in Figure 12, we observe a linear relationship between the number of objects and the generation speed. Although the inference time naturally increases as the scene becomes more cluttered, the decline in speed remains gradual and stable. This demonstrates that our approach scales effectively and maintains practical efficiency even when handling scenarios with a large number of instances.

G. Illustration of Noise in SACap-1M

The comparison in Figure 13 illustrates the annotation noise inherent in the SACap-1M (Li et al., 2025c) dataset

where images are resize to 1:1 for better view. SACap-1M generates regional captions by prompting the Qwen2-VL-72B (Bai et al., 2025) model with bounding box coordinates. However, this box-based prompting mechanism inevitably introduces noise, as rectangular bounding boxes rarely align perfectly with irregular object shapes. Consequently, the boxes often encompass background elements or adjacent instances, leading the VLM to erroneously attribute these surrounding visual features to the target entity.

To address this limitation, we utilize DescribeAnything (Lian et al., 2025) to perform precise mask-level annotation. By constraining the visual analysis strictly to the segmented regions, our approach effectively filters out context-induced noise (highlighted by the blue marks in the Figure 13). As a result, SA-Z derives significantly cleaner and more detailed captions that strictly adhere to the visual attributes of the specific instances of interest.

H. Examples of SA-Z

Figure 14 provides examples of the training dataset sampled from SA-Z. Our dataset provides detailed annotations for mask areas and pairwise instance occlusion relationships. We also incorporate SAM-3D (Chen et al., 2025) to extract the amodal annotations for the occluded instance.

I. Examples and Statistics of the SA-Z Eval

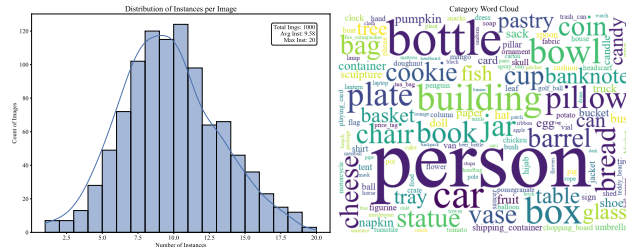


Figure 16. Statistical overview of SA-Z Eval. The left shows the distribution of instances per image, while the right word cloud illustrates the semantic diversity across 749 categories.

Figure 16 presents key statistics of our SA-Z Eval benchmark. As shown in the statistical plots, the benchmark encompasses 749 distinct categories with varying instance densities per image, ensuring both semantic breadth and scene complexity. To ensure consistency with OverLayBench (Li et al., 2025b), we employ Qwen-VL-32B (Bai et al., 2025) to generate semantic labels and filter out non-salient objects from SA-1B (Kirillov et al., 2023). The examples are in Figure 15. Notably, we adopt modal bounding boxes for evaluation instead of amodal ones to minimize ambiguity. Since amodal boxes encompass occluded regions that lack corresponding visual pixels, using them for spatial metrics like IoU would introduce misalignment with the generated content, whereas modal boxes provide a more grounded reference for evaluating visual layout accuracy.

OcclusionFormer: Arranging Z-Order for Layout-Grounded Image Generation



Figure 10. The visual comparison of different methods on the OverLayBench (Li et al., 2025b).



Figure 11. The visual comparison of different methods on our constructed SA-Z Eval.

SACap-1M	SA-Z	Mask
<p>A. A green and yellow soccer ball with a blue and white emblem on it. B. A soccer ball with pixelated designs on a green surface, with two flags in the background. C. A circular emblem with yellow and red sections. D. A soccer ball with black and white hexagonal patterns is placed on a green surface. E. A green grassy surface with some small white spots, likely dew or light reflections.</p>	<p>A. A circular flag with a green field and a yellow diamond in the center. Inside the yellow diamond, there is a blue globe with white stars and a white band across it. B. The background is a dark, textured surface with a subtle gradient of blue and green hues. It has a slightly mottled appearance, giving it a dynamic and vibrant look. C. A circular flag with three vertical stripes of equal width. From left to right, the colors are black, yellow, and red. D. A white soccer ball with a pattern of black and teal geometric shapes, featuring a mix of pentagonal and hexagonal panels. E. The grass is a lush, vibrant green with a dense, even coverage. The blades are short and uniformly cut, creating a smooth, well-maintained appearance.</p>	
<p>A. A wooden table with a vase of dried flowers, a glass of orange juice, a sandwich, sunglasses, and a book titled "KINFOLK." B. A laptop computer with a dark screen is placed on the couch. C. A vase with dried plants on a wooden table. D. A glass filled with a light-colored liquid, possibly a drink, sits on the table. E. A cozy indoor setting with a wooden table featuring a vase with dried plants, a drink, a sandwich, sunglasses, and a laptop on a leather couch. F. A piece of bread with greens on top, placed on a white paper on the table. G. A plate with greens and bread on a wooden table. H. A dark green leather sofa with a laptop on it. I. A book with the title "KINFOLK" and an image of greenery on its cover. J. A wooden lamp with a metal stand is positioned near the table.</p>	<p>A. A wooden table with a smooth, polished surface showcasing natural wood grain patterns and a warm, medium brown tone. B. A black laptop with a matte finish, featuring a screen displaying a webpage with a blue header and a small image. C. A tall, slender vase with a narrow neck and a wider base, featuring a natural wood grain pattern in shades of brown and tan. D. A clear glass with a thick base and vertical ridges along the sides. The glass contains a layered beverage with a creamy, light brown top layer and a white bottom layer. E. The wall is painted in a light blue color and features a smooth, flat surface. It has a vertical seam running down the left side, indicating a possible joint or division in the wall. F. A piece of white, crumpled tissue paper with irregular edges and a slightly translucent appearance. G. A cluster of fresh, green arugula leaves with a slightly crinkled texture, interspersed with small, reddish-brown leaves. H. A dark leather sofa with a tufted backrest and seat cushions, featuring a rolled armrest on the left side and visible stitching details. I. A white book with the title "KINFOLK" printed in large, bold, black letters at the top. J. A floor lamp with a slender, cylindrical metal pole that transitions from a darker shade at the top to a lighter shade towards the bottom.</p>	
<p>A. The sky is visible above the building, with a bright and clear appearance. B. A statue of a figure holding a flag stands in front of an ornate building with arched windows and stone details. C. A statue holding a flag stands in front of an old building with arched windows. D. A statue of a person holding a flag stands in front of an old building with arched windows.</p>	<p>A. The sky is a pale, almost white, light blue with a smooth gradient, transitioning from a slightly darker blue at the top to a lighter blue towards the bottom. B. The building features a series of tall, arched windows with red frames, set within a stone facade. The windows are arranged in a symmetrical pattern, with each window having a pointed arch at the top. C. A weathered, dark green flag with a slightly frayed edge, attached to a vertical pole. The flag appears to be made of a fabric material, showing signs of wear and discoloration. D. A bronze statue of a robed figure with a flowing, textured garment. The figure's right arm is extended outward, holding a flagpole with a flag that is partially visible.</p>	
<p>A. A stone floor with people walking on it. B. A stone statue of a seated figure with multiple heads, located inside an ancient temple with sunlight streaming through windows. C. A person wearing a red shirt and blue jeans is standing near the statue. D. A woman wearing a red shirt and white pants stands near the statue. E. A large stone statue of a seated figure with intricate carvings and multiple faces on top.</p>	<p>A. The stairs are constructed from wooden planks arranged horizontally. The planks are weathered, showing signs of age and wear, with visible grain and texture. B. The temple features a stone wall with intricate carvings, including a series of vertical, wavy patterns on the left side. C. A woman with shoulder-length brown hair, wearing a white t-shirt with a colorful graphic design on the front, blue denim capri pants, and black sandals. D. A girl with long, dark hair tied back in a ponytail, wearing a red and white patterned short-sleeve shirt and white capri pants. E. A stone sculpture of a seated figure with a serene expression, adorned with a detailed headdress and a draped garment.</p>	
<p>A. The sky is blue with some clouds. B. A statue of a person with intricate clothing and jewelry, standing between two other statues. C. A stone pedestal with plaques and statues of three figures in traditional attire. D. A black and white cloth is hanging from the building. E. Three statues in traditional attire stand before a building with a red-tiled roof and white walls. F. Statue of a person with intricate clothing and headdress, standing on a pedestal in front of a building with a red-tiled roof. G. A statue of a person wearing traditional attire and jewelry, standing with arms extended.</p>	<p>A. The sky is a soft, pale blue with a few faint, wispy clouds scattered across it. The clouds are thin and elongated, blending gently into the blue background. B. A dark bronze statue of a standing figure adorned with intricate jewelry and traditional attire. The figure wears a detailed headdress with a pointed top and a decorative band around the head. C. The monument features a rectangular base with a smooth, light-colored surface. It has three rectangular plaques, each with a white background and yellow text. D. A black and white curtain featuring a black upper section with a pattern of vertical stripes and a white lower section with a smooth texture. E. The house features a white exterior with a red-tiled gable roof. It has two visible windows with wooden shutters, one on the left and one on the right. F. A bronze statue of a standing figure adorned in traditional attire, featuring a detailed headdress with intricate patterns. G. A bronze statue of a standing figure adorned in traditional attire, featuring a detailed headdress with intricate patterns.</p>	
<p>A. A light-colored wooden floor with a white laptop on it. B. A person wearing a plaid shirt and black pants is sitting on a couch with a laptop on their lap. C. A person with long hair wearing a white shirt and a watch on their wrist. D. A silver laptop computer being used by a person sitting on a couch. E. The image shows two people sitting on a couch with a laptop. One person is wearing a plaid shirt and the other has long hair. F. A white couch with two people sitting on it, one wearing a plaid shirt and the other in a white top.</p>	<p>A. The floor is composed of light gray wooden planks with a smooth, matte finish. The planks are laid out in a parallel arrangement, running horizontally across the image. B. A man with short, dark hair is wearing a white t-shirt with the word "STREET" printed in black on the front. C. A girl with long, straight brown hair, wearing a white top and a blue and yellow plaid shirt. She has a gold watch on her left wrist. D. A silver laptop with a smooth, matte finish on the back of the screen. The laptop has a thin profile with rounded edges and a slightly raised hinge area. E. The wall is smooth and painted in a light, neutral color. It has a vertical seam running down the right side, indicating a possible joint or division in the wall. F. The couch features a light beige fabric upholstery with a smooth texture.</p>	

Figure 13. The comparison of captions between SACap-1M (Li et al., 2025c) and SA-Z (Ours).

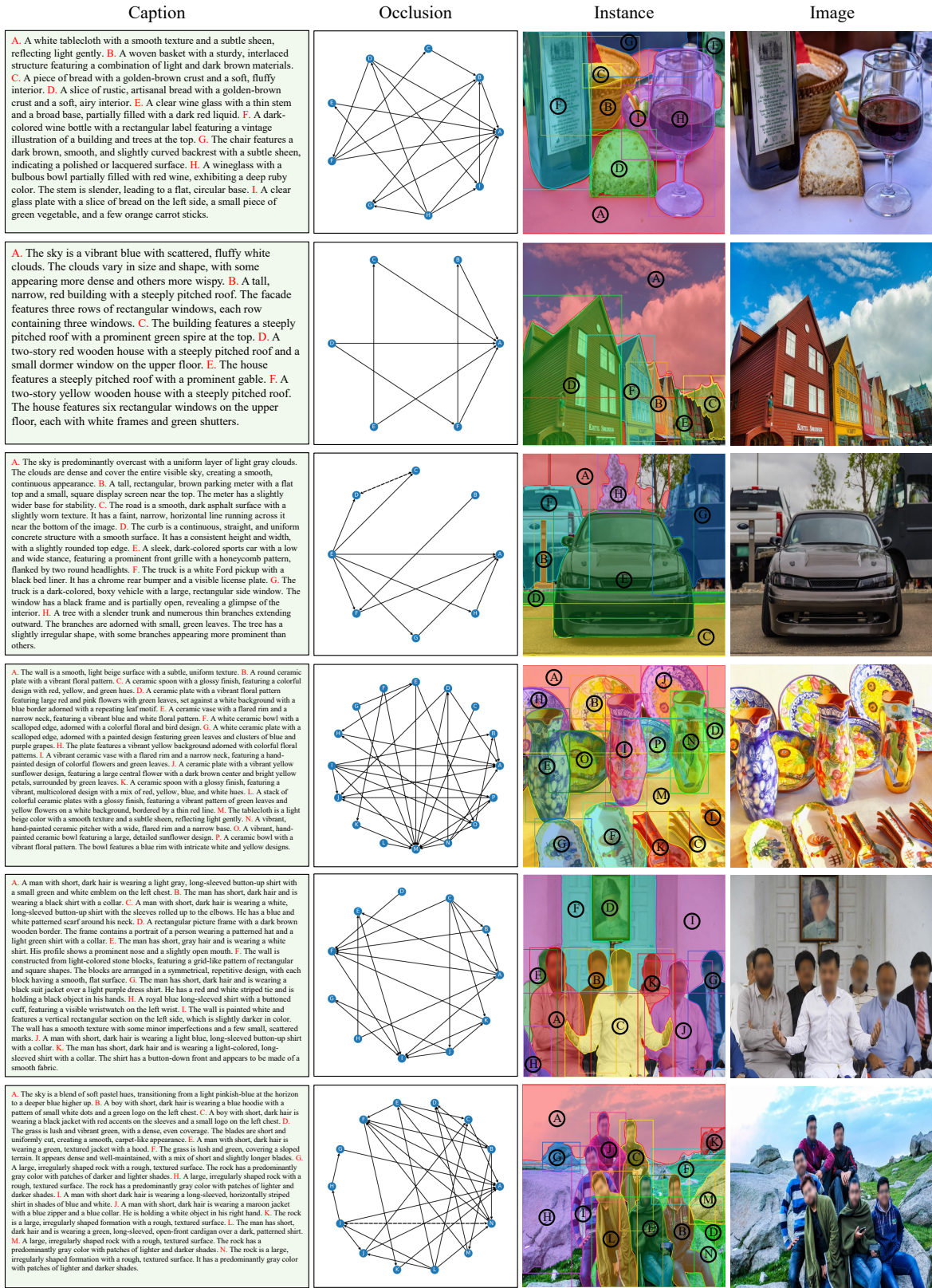


Figure 14. Examples from SA-Z, where arrows in the occlusion graphs denote the “occludes” relationship.

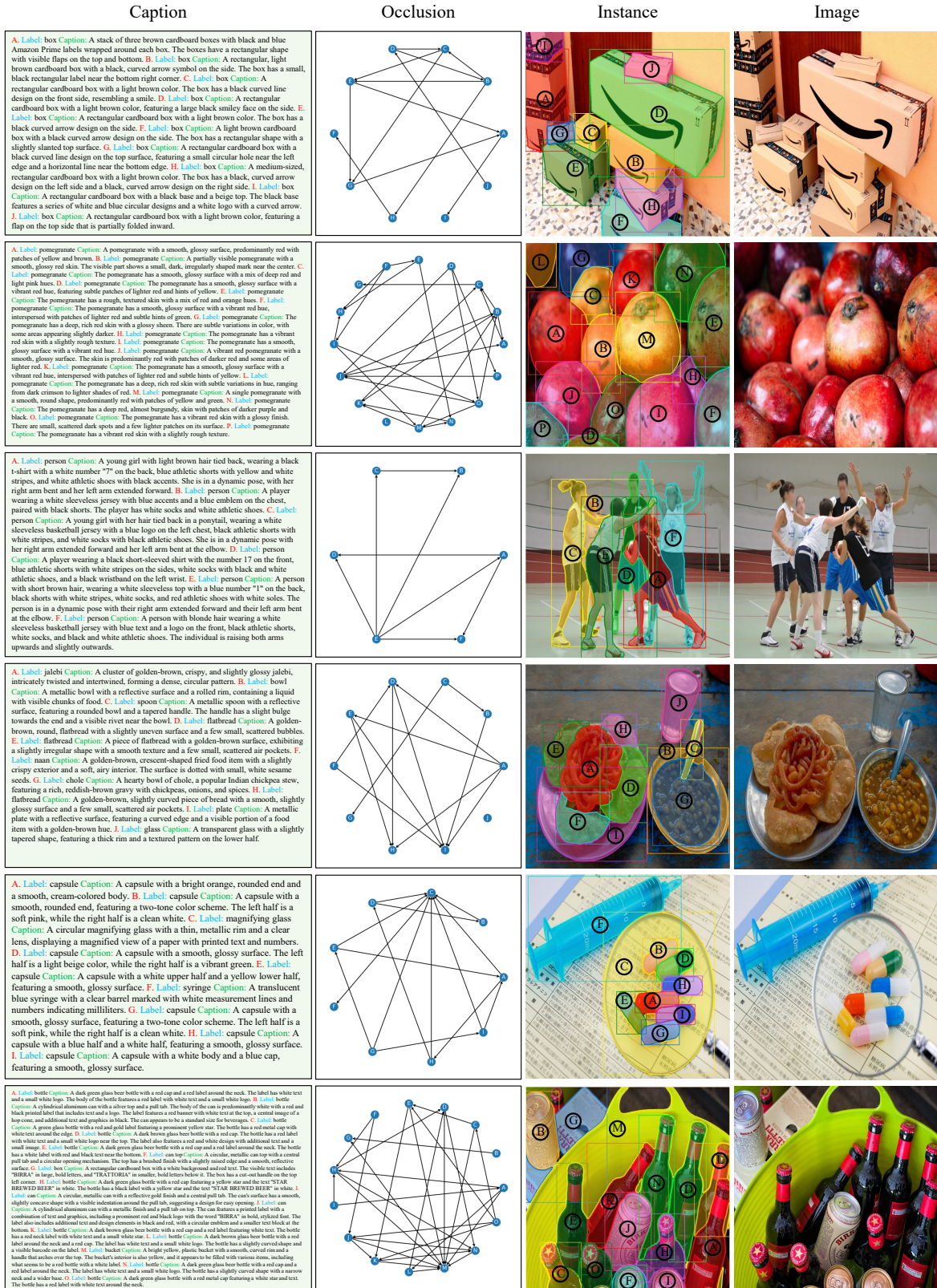


Figure 15. Examples from our created SA-Z Eval, where arrows in the occlusion graphs denote the “occludes” relationship.